Chemoselective reduction of quinoline over Rh-C 60 nanocatalysts

Zhishan Luo, Yuanyuan Min, Wolfgang Bacsa, Divya Nechiyil, Yann Tison, Hervé Martinez, Pierre Lecante, I.C. Gerber, Philippe Serp, M. Rosa Axet

Chemoselective reduction of quinoline over Rh-C_{60} nanocatalysts

Zhishan Luo,[a] Yuanyuan Min,[a] Divya Nechiyil,[b] Wolfgang Bacsa,[b] Yann Tison,[c] Hervé Martinez,[c] Pierre Lecante,[b] Iann C. Gerber,[d] Philippe Serp,[a] and M. Rosa Axet[a*]

[a] LCC-CNRS, Université de Toulouse, CNRS, INPT, Toulouse, France

[b] Centre d'élaboration des matériaux et d'études structurales UPR CNRS 8011, 29 Rue Jeanne-Marvig, BP 4347, 31055 Toulouse, France

[c] CNRS/UNIV PAU & PAYS ADOUR/E2S UPPA, Institut des sciences analytiques et de physicochimie pour l'environnement et les matériaux, UMR5254, 64000, Pau, France.

[d] LPCNO, Université de Toulouse, INSA-CNRS-UPS, 135 Avenue de Rangueil, 31077 Toulouse, France

rosa.axet@lcc-toulouse.fr

ABSTRACT

The design and engineering of heterogeneous nanocatalyst that are both highly active and selective for hydrogenation reactions constitute a crucial challenge. In that context, herein a series of Rh-C_{60} nanocatalysts have been synthesized *via* the decomposition of an organometallic rhodium complex in the presence of fullerene C_{60} under H_2 atmosphere. Rhodium atomically dispersed or rhodium nanoparticles on Rh-C_{60} spherical fulleride particles were produced by tuning the Rh/C_{60} molar ratio. A significant charge transfer between rhodium and C_{60} was evidenced through Raman and X-ray photoelectron spectroscopy, which indicates electron-deficient Rh species. The resulting heterostructured nanomaterials were applied successfully in the catalytic hydrogenation of quinoline, exhibiting excellent activity and producing selectively the partially hydrogenated product, 1,2,3,4-tetrahydroquinoline. Density functional theory (DFT) calculations show that the hydride coverage of the Rh NP plays a key role in the adsorption modes of quinoline and 1,2,3,4-tetrahydroquinoline on the surface of the NP, and that these adsorption modes are modulated by the presence of fullerene C_{60}, thus affecting the activity and selectivity obtained with this rhodium based catalyst.

KEYWORDS

rhodium, nanoparticles, ligand effects, catalysis, quinoline, hydrogenation

INTRODUCTION

Heterogeneous catalytic hydrogenation reaction is broadly acquainted with one of the most fundamental chemical transformations in both laboratory and industry.[1-5] Over the years, numerous heterogeneous nanocatalysts, in particular, carbon-based hybrid nanostructures, have shown high catalytic activity and selectivity in hydrogenation reactions,[6-12] owing to their high surface area to volume ratio, exclusive electronic properties to favour charge transfer, high chemical and thermal stability, easy recovery from the reaction mixture and high mechanical strength. Catalytic reduction of quinoline (**1**) is a key organic reaction where one of the products, 1,2,3,4-tetrahydroquinoline (**2**), is an important intermediate for pharmaceuticals, agrochemicals, alkaloids and various biological active molecules.[13-16] Specially, quinolines allow preparing tetrahydroquinoline products that are broadly found in drug molecules.[14,16] A simple and effective strategy of synthesis is the direct regioselective hydrogenation of quinoline (Scheme 1). However, 5,6,7,8-tetrahydroquinoline (**3**) and the fully hydrogenated product decahydroquinoline (**4**) may be also produced.

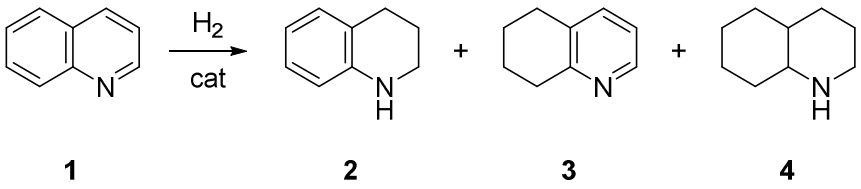

Scheme 1. Hydrogenation of quinoline.

A variety of heterogeneous catalysts have been developed to improve activity and selectivity for this reaction in recent years. Au,[17] Rh,[18-25] Ru,[26,27] Pd[28] and Pt[29] -based catalysts have revealed to be very active and selective. Specifically, Rh nanoparticles (NP) show high selectivity towards 1,2,3,4-tetrahydroquinoline (**2**). For instance, rhodium NP immobilized in a Lewis acidic ionic liquid (IL) catalyse a large scope of heteroarenes, being very selectively to the arene ring without hydrogenating other functional groups.[23] In the specific case of quinoline, it was selectively hydrogenated to **2** (95% yield) at 30 bars of H_2 and 80°C after 15 h of reaction. Other Rh catalysts have produced the partial

hydrogenated product **2** very selectively under similar reaction conditions: Rh NP over reduced graphene oxide (99% yield; 30 bar of H_2, 80°C, 12h);[25] Rh NP stabilized with polyethylene glycol (99% selectivity; 30 bar of H_2, 100°C, 3h);[22] Rh NP stabilized with a phosphine-functionalized IL (99% selectivity; 30 bar of H_2, 50°C, 5h);[21] or Rh NP stabilized with tannin (94% selectivity; 20 bar of H_2, 80°C, 0.5h).[19] Interestingly, Rh/AlO(OH)[18] catalyst and Rh NP stabilized with an N-heterocyclic carbene (NHC)[24] were able to hydrogenate quinoline under milder reaction conditions. Rh/AlO(OH) was active at room temperature using a hydrogen balloon and produced **2** with a selectivity of 94% after 6h of reaction. Rh-NHC was also active at low temperature (30°C) under 20 bar of H_2 pressure reaching full conversion after 140 min of reaction, but in this case only 75% of selectivity to **2** was observed (TOF= 238 h^{-1}). Full conversion after only 30 min of reaction was achieved by increasing the temperature to 60°C, quinoline was completely consumed with 75% of selectivity towards **2**; after 24 hours of reaction the fully reduced product **4** was obtained (TOF= 496 h^{-1}). These two last examples describe very active catalysts able to produce the fully hydrogenated decahydroquinoline (Rh/AlO(OH) under slightly harsher reaction conditions (8 bar of H_2, 100°C, 5h);[20] which is in opposition with the findings using Rh NP immobilized in a Lewis acidic (IL).[23] These results suggest that electron-rich Rh NP are very active, but, in general, less selective to the partially hydrogenated product **2**.

On the other hand, electron-poor Ru NP can be produced straightforward from the decomposition of (1,5-cyclooctadiene)(1,3,5-cyclooctatriene)ruthenium(0) [Ru(COD)(COT)] with H_2 in the presence of fullerene C_{60}.[30] This nanocatalyst shows excellent activity and selectivity in the hydrogenation of nitrobenzene.[31,32] The same methodology has been used to obtain other metal NP.[33] Also, fullerene C_{60} based catalysts with other metals have been described,[34] including Pd,[35] Ni[36] and Ru.[37,38] With the ability of fullerene to accommodate various metals,[39] as well as, the effectiveness of the organometallic approach to produce almost any kind of noble metal NP, we decided to synthesize Rh-C_{60} catalysts with the aim to produce electron-poor Rh NP, which can be very interesting for selective quinoline hydrogenation.[23,25] In this work, we demonstrate that rhodium NP can be synthesized straightforwardly *via* the decomposition of the [$Rh(\eta^3\text{-}C_3H_5)_3$] complex in the presence of fullerene C_{60} in 1, 2-dichlorobenzene (DCB) under H_2 atmosphere. Rh atomically dispersed or Rh NP on Rh-C_{60} fulleride spherical particles were produced by tuning the ratio of the Rh precursor and fullerene. These Rh

compounds where characterized using several techniques such as transmission electron microscopy (TEM), wide angle X-ray scattering (WAXS), inductively coupled plasma optical emission spectroscopy (ICP-OES), attenuated total reflection infrared spectroscopy (ATR-IR), solid-state NMR (SSNMR), and thermal gravimetric analysis (TGA), including X-ray photoelectron spectroscopy (XPS) and Raman spectroscopy, which evidenced a charge transfer from rhodium to fullerene. The nanostructures were used as catalyst in the hydrogenation of quinoline, showing excellent activity (TOF= 488.0 h^{-1}) and selectivity to **2** (up to 98%). Density Functional Theory (DFT) calculations were also performed to support those findings.

RESULTS AND DISCUSSION

A series of Rh-C_{60} compounds was synthesised trough decomposition of [Rh(η^3-C_3H_5)$_3$] under 3 bars of H_2 atmosphere in the presence of C_{60} using 1, 2-dichlorobenzene (DCB) as solvent at 50 °C. In this series, the molar Rh/C_{60} ratio has been varied ranging from [Rh]/[C_{60}] = 1 to 20. Figure 1 shows representative TEM images of the as-synthesised products. Nanospheres with a size of about 100-170 nm were observed, which were decorated with Rh NP (Figure 1, Figure S1 and Table 1). The NP size was in the range of 2-3 nm, presenting a broad size distribution (polydispersities around 30%), displaying a bimodal distribution for samples 5/1 and 10/1. These species are structurally similar to the ruthenium nanocatalysts stabilized with fullerene C_{60} described in a previous study by some of us.[30] In this above-mentioned work, the decomposition under dihydrogen of [Ru(COD)(COT)] in the presence of fullerene C_{60} provided Ru based catalyst composed by Ru-C_{60} molecular spheres with the surface decorated with Ru NP; as pointed out by a combination of characterization techniques including TEM, WAXS, Extended X-Ray Absorption Fine Structure (EXAFS), and supported by DFT calculations. Also, Ru-C_{60} fulleride nanospheres synthesised in DCB displayed a size of 200.0 ± 38.5 nm , which is similar to the ones of Rh-C_{60} materials. Furthermore, HRTEM analyses were performed for Rh-C_{60} 1/1 and 10/1 samples. The HAADF-STEM mode allowed to detect in the Rh-C_{60} 1/1 compound a few Rh NP on the surface of the nanospheres, together with isolated atoms on the surface, which was in contrast with the analyses carried out for the Rh-C_{60} 10/1 sample; for which the Rh NP on the surface were more abundant (Figure 2). In addition, the distribution of the Rh signal by EDX analysis along the line scan is uniform for the sample 1/1 (Figure 2) while it confirms the presence of Rh NP on the surface of Rh-C_{60} 10/1, as higher

Rh content was detected on the surface of the sphere. The ICP analyses pointed out that rhodium content was lower than expected, which suggested the presence of residual DCB on the samples, further corroborated by IR, SSNMR and TGA, as it will detailed bellow.

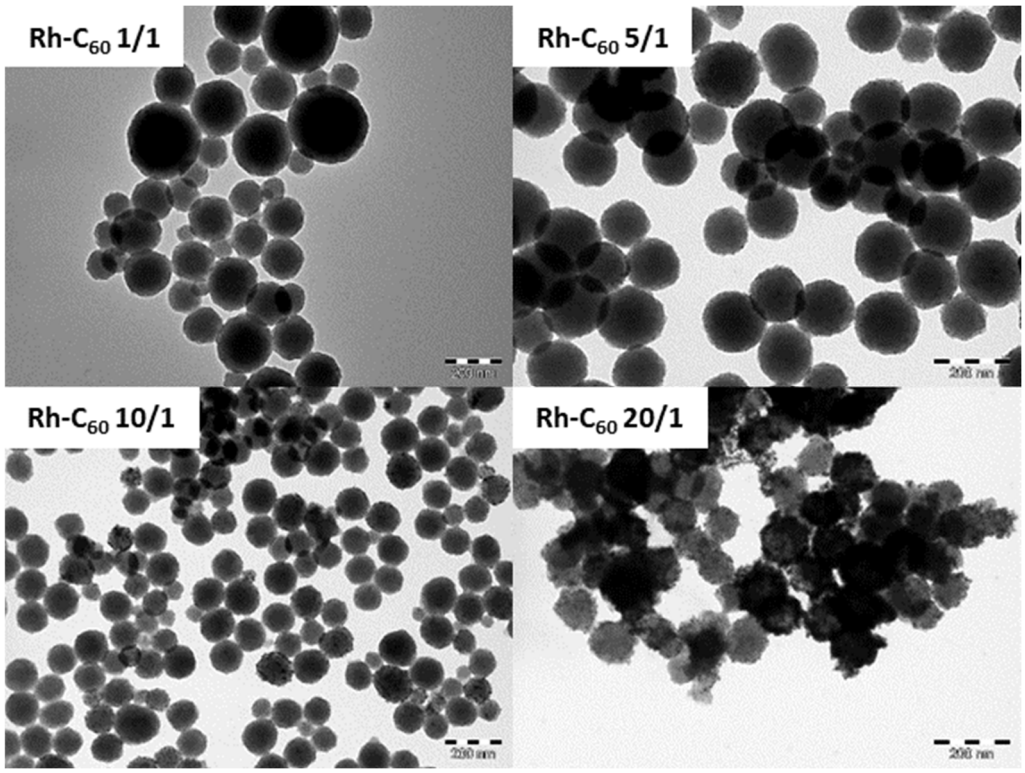

Figure 1. TEM micrographs of Rh-C_{60} 1/1; 5/1; 10/1; and 20/1 (scale bar 200 nm).

Table 1. Mean size distributions and rhodium content of the Rh-C_{60} nanocatalyst.

Rh-C_{60}	Rh content (%)[a]	NP mean size (nm)[b]	Nanospheres mean size (nm)[b]
1/1	9.2	2.0 ± 0.4	158.2 ± 27.5
5/1	23.3	1.1 ± 0.3 (21%)/ 3.0 ± 0.9 (79%)[c]	103.0 ± 15.5
10/1	35.9	1.9 ± 0.5 (69%)/ 4.7 ± 1.1 (31%)[c]	167.9 ± 27.3
20/1	46.2	2.3 ± 0.6	96.3 ± 14.4

[a]By ICP. [b]Manual measurement from enlarged TEM micrographs of at least 150 objects. [c] In brackets percentage of each population

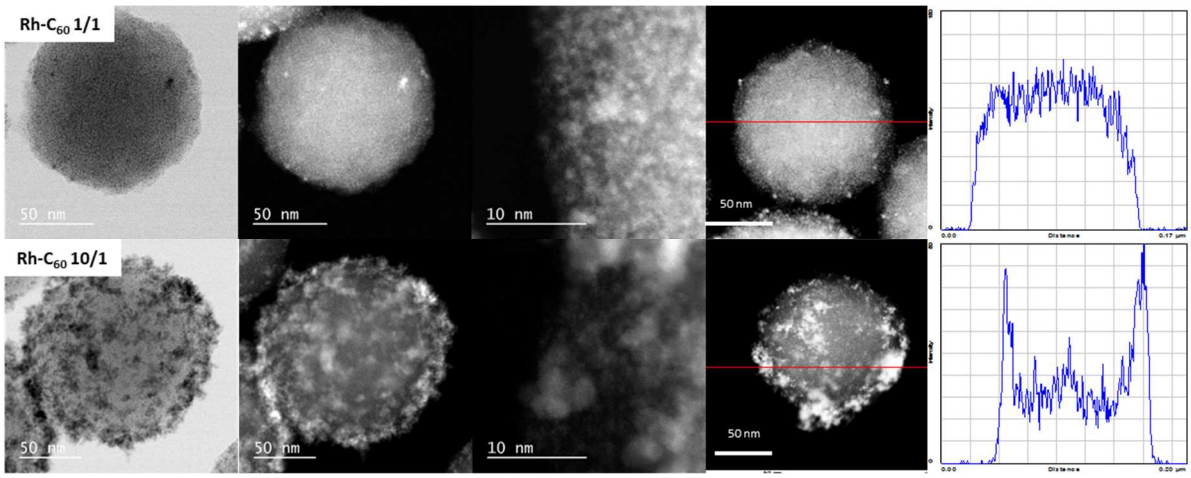

Figure 2. STEM-HAADF images of Rh-C_{60} 1/1 (top) and Rh-C_{60} 10/1(bottom) together with the EDX line scanning profile of Rh signal extracted from cumulated EDX spectra on the line scans (left) (scale bars from left to right: 50 nm, 50 nm, 10 nm and 50 nm).

In order to obtain more insight on the evolution of these Rh-C_{60} species during the synthesis, the reaction was monitored by *ex situ* TEM analyses. For that, the decomposition of [Rh(η^3-C_3H_5)$_3$] under hydrogen in the presence of fullerene C_{60} (Rh/C_{60} = 10/1) was performed at low temperature (-20 °C). The reaction mixture was sampled over time and the TEM images are displayed in Figure S2 together with their respective size histograms. The evolution of the nanostructures over time showed that at 2 min of reaction worm-like structures composed by nanospheres were already formed, with a nanosphere mean size of 218.7 ± 23.9 nm, which evolved to independent nanospheres after 5 min of reaction displaying larger mean size, 274.4 ± 33.1 nm (Table S1). Rh nanoparticles were observed after 15 min of reaction on the surface of the nanospheres as well as dispersed on the TEM grid, 1.7 ± 0.5 and 3.4 ± 1.3 nm, respectively. The reaction was allowed to react overnight at -20°C and the last TEM analysis performed showed that the size of the nanospheres remained similar, 255.7 ± 39.5 nm; while the Rh NP on the surface presented a bimodal distribution, 2.4 ± 0.7 and 4.7 ± 0.4 nm, and isolated NP were no longer observed. These observations make feasible to propose that, as previously observed during the synthesis of Ru-C_{60} compounds,[30] the nanospheres are composed by molecular species, which form this particular shape due to the stirring and the different viscosity between the as-synthesized species and the solvent.[40] For previously described Ru-C_{60} species, lower solvent viscosity

lead to smaller nanospheres. Here, the decrease of the temperature to -20°C increased the size of the nanospheres when compared to the synthesis performed at 50°C (255.7 ± 39.5 nm for -20°C, 103.0 ± 15.5 nm for 50°C). Taking into account that the viscosity increases when the temperature decreases, an increase of the diameter is expected, as observed here. Also, the detection of isolated NP at 15 min could indicate that a double NP nucleation is occurring during the synthesis: one on the surface of the Rh-C_{60} nanospheres, and a second one in solution. It is possible that the rhodium precursor reacts with the solvent, as arene-rhodium complexes have been described in the past.[41-43] The arene ring of DCB being electro-deficient, it should coordinate weakly when compared to other arene compounds such as benzene or toulene,[43] producing also NP under reaction conditions. In addition, the fact that the Rh NP are stabilized by a weakly stabilizing ligand (DCB) could also explain that the isolated NP observed first are then adsorbed on the surface of the nanospheres, explaining in turn the bimodal size distributions and the polydispersity (around 30%) of the samples.

WAXS analyses were performed in the Rh nanostructures. After corrections and Fourier Transform, the Radial Distribution Function was obtained (RDF, Figure S3). For the lowest Rh amounts (*i.e*. 1/1 and 2/1) the observed RDFs present only weak features actually dominated by the distances in C_{60}. From 5/1, the distances are consistent with metallic Rh in the *fcc* structure and both amplitude and coherence length increase in relation with the Rh amount. Coherence lengths could be estimated to 3.3 nm for 5/1, 3.5 nm for 10/1 and 3.8 nm for 20/1. It should be noted that the scattering phenomenon strongly emphasizes the contribution of larger particles, which does not make it very sensitive to size distribution. This behaviour has been previously observed for Ru-C_{60} species.[30]

To gain further insight into the interactions between Rh and fullerene, XPS analyses of Rh-C_{60} 1/1 and 10/1 were conducted (Figure 3, Figure S4 and Table S2). Peaks in the full XPS spectra indicate the presence of Rh, C and O elements on both samples (Figure S4). Rh 3d peaks could be fitted into a unimodal doublet, pointing to the presence of only one Rh chemical state: metallic Rh^0. In the Rh 3d region of the Rh-C_{60} 1/1 XPS spectrum, a single doublet is observed at 307.8 eV ($3d_{5/2}$) and 312.4 eV ($3d_{3/2}$). These binding energies may evidence a charge transfer from the metal to C_{60} molecules, since they are significantly shifted compared to that of metallic rhodium (Rh $3d_{5/2}$ component at 307.2 eV).[44]

The Rh 3d core peaks of Rh-C_{60} 10/1 are asymmetric and appear at relatively lower binding energies *i.e.* 307.2 eV ($3d_{5/2}$) and 311.9 eV ($3d_{3/2}$), which are typical of metallic Rh^0. Such an asymmetry could be explained by the presence of a second contribution at slightly higher binding energies, consistent with the charge transfer mentioned above. In agreement with the EDX results presented earlier, the atomic percentage (Table S2) for rhodium is higher for Rh-C_{60} 10/1 (8.0 %) than Rh-C_{60} 1/1 (1.5%). For both samples, the C 1s peaks (Figure S4 and Table S2) are dominated by a peak at 284.3 eV attributed to fullerene C_{60}, with less intense peaks associated with contaminating carbon (285.0 eV), oxygenated carbon groups (between 286 and 288.5 eV) and a shake-up peak (at *ca*. 290.0 eV). It is to be noted that the binding energy of 284.3 eV is significantly lower than the value reported for the C 1s peak of fullerene films thicker than one monolayer (approximately 284.8 eV).[45] This shift is consistent with the charge transfer mentioned above, as observed for a 1-monolayer-thick film of C_{60} on Cu(111).[45] The O 1s peaks (Figure S4 and Table S2) for both samples correspond to oxygen atoms bound to carbon.

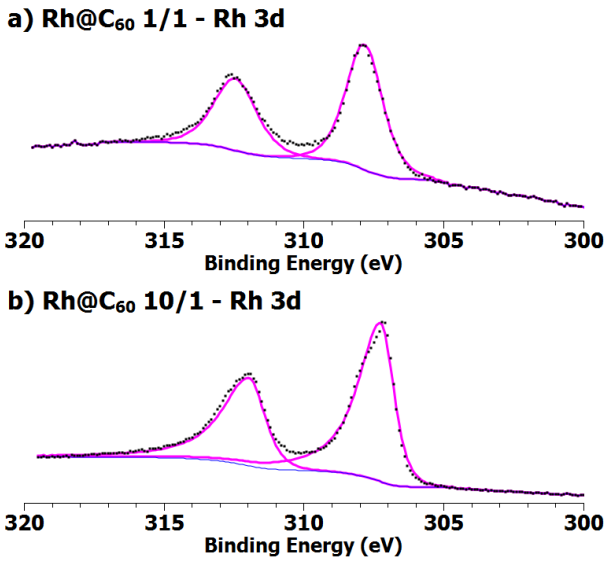

Figure 3. XPS Rh 3d spectra of a) Rh-C_{60} 1/1 and b) Rh-C_{60} 10/1.

Raman spectroscopy is an efficient technique to study C_{60} as it can provide important information on various vibrational modes and thereby one can understand the crystallinity, structure, intramolecular bond formation and molecular deformation. The C_{60} molecule has 46 intramolecular modes, among which 10 are Raman active (2 Ag + 8 Hg). The Ag (1) mode at ~492 cm^{-1} is known as the breathing mode, which originates from the in phase radial movement of all sixty carbon atoms in the icosahedral

structure. The second Ag mode Ag (2), situated at 1458-1468 cm^{-1} is also known as the pentagonal pinch mode corresponding to the in phase tangential displacement of carbon atoms, leading to an out of phase breathing mode of pentagons and hexagon faces. Similarly, the low frequency Hg modes (<700 cm^{-1}) mainly arise from the radial molecular movement, whereas higher frequency Hg modes are mainly due to the tangential displacements.[46,47] The Raman spectrum of C_{60} displays intense tangential Raman modes of vibrations such as Ag (2), Hg (7), and Hg (8) at 1459 cm^{-1}, 1429 cm^{-1}, and 1561 cm^{-1} respectively. Figure 4 shows the Raman spectra of Rh-C_{60} samples with different Rh/C_{60} ratios and Table 2 lists the peak position, peak shift and full width half maxima (FWHM) as a function of the Rh/C_{60} ratios, which are obtained by peak fitting using the Lorentzian function. It is observed that after Rh introduction, the peaks are broadened with decrease in intensity as well as increase in luminescence background. The Ag (2) and Hg (7) peaks depict downshifts, whereas the Hg (8) shows an upshift as compared to the corresponding C_{60} peak positions. The FWHM of the rhodium containing samples are considerably larger compared to the C_{60} fullerene. For the Rh-C_{60} samples, the low frequency vibrations are not clearly visible because of a large luminescence background and due to the softening of these modes. The shifts in the tangential modes at higher wavenumber have been assigned in literature to the electron transfer from dopants to the C_{60} molecule.[48] The broadening of these prominent modes, mainly those of Hg (7) and Hg (8) are explained by the electron-phonon coupling due to doping. The broadening of Ag (2) mode is explained by the expansion of C_{60} molecule, which reduces the force constants.[48] The reported electron transfer for the downshift of tangential modes of vibrations at higher wavelength are -6 cm^{-1}/electron for Ag (2), -7 cm^{-1}/electron for Hg (7) and -15 cm^{-1}/electron for Hg (8).[49] The downshift of pentagonal pinch mode is commonly used to quantify the charge transfer from the metal to the antibonding electron orbitals of the C_{60} molecule since it is the most intense peak in the Raman spectra of C_{60}. Whereas, Rh-C_{60} 10/1 shows a higher downshift of -26.3 cm^{-1} corresponding to an electron transfer of ~4.4 e^- and Rh-C_{60} 20/1 exhibits a downshift of -23.5 cm^{-1} corresponding to an electron transfer of ~3.9 e^-. For Rh doping, the negative shift and broadening increases up to 10/1, but decreases for 20/1, and from this we can predict that there is saturation with respect to Rh doping.

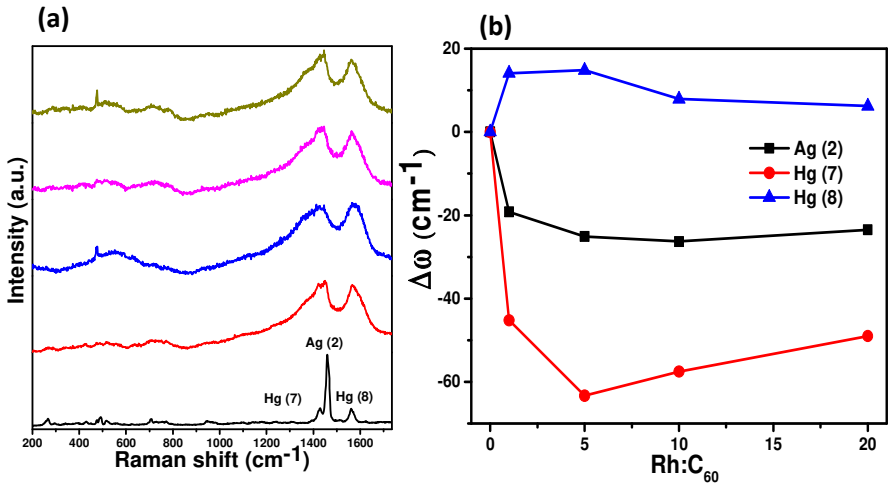

Figure 4. a) Raman spectra of C_{60} fullerene together with Rh-C_{60} nanostructures and b) shift in peak position *vs.* Rh/C_{60} ratio.

Table 2. Peak position, shift of peaks and FWHM of C_{60} and Rh-C_{60}

	Ag (2)			Hg (7)			Hg (8)		
	Position (cm^{-1})	Shift (cm^{-1})	FWHM	Position (cm^{-1})	Shift (cm^{-1})	FWHM	Position (cm^{-1})	Shift (cm^{-1})	FWHM
C_{60}	1459.1	0	15.1	1423.6	0	17.2	1563.2	0	20.1
Rh-C_{60} 1/1	1439.9	-19.2	65	1378.4	-45.2	206.4	1577.3	14.1	84.6
Rh-C_{60} 5/1	1434. 0	-25.1	105.6	1360.3	-63.3	181.5	1578.0	14.8	81.2
Rh-C_{60} 10/1	1432.8	-26.3	71	1366.1	-57.5	267.1	1571.1	7.9	82.85
Rh-C_{60} 20/1	1435.6	-23.5	61.1	1374.6	-49	239.8	1569.4	6.2	77

The ATR-IR spectra of the Rh-C_{60} nanostructures were recorded in the solid state (Figure S5-a)). Characteristic peaks of the fullerene C_{60} are observed at 518, 577, and 1182 cm^{-1}, which confirm the presence of the stabilizing molecule in the samples. Other intense peaks are attributed to the presence of DCB (657, 745, 1033, 1124, 1432 and 1454 cm^{-1}). The SSNMR of the Rh-C_{60} 10/1 (Figure S6) confirmed the presence of fullerene C_{60}, whose signal appears at 147.1 ppm. The MAS $^{13}C\{^{1}H\}$ NMR also show two signals at 130.9 and 128.1 ppm, which were attributed to remaining DCB and corroborated the presence of the solvent in the samples as seen in the ATR-IR spectra. The CP-MAS ^{13}C NMR (CP = ^{1}H–^{13}C cross polarization) allowed to observe a broad signal centered around 43 ppm attributed to a mixture hydrogenated fullerene species. The hydrogenation of fullerene C_{60} at ambient temperature and pressure has already been reported for Rh/Al_2O_3 catalyst,[50] the formation of these hydrogenated

species were also observed for Ru-C_{60} materials.[30] Adsorbed DCB was removed by annealing the samples at 200°C under Ar. The ATR-IR spectra (Figure S5-b)) recorded on the heat-treated samples show that DCB peaks vanished. Additionally, TGA analyses (Figure S7) confirmed the efficiency of the thermal treatment. No appreciable structural change of the nanospheres was observed from TEM analyses on Rh-C_{60} 5/1 sample (denoted as Rh-C_{60} 5/1 TT) (Figure S8); however, the size distribution of the NP was unimodal, centred at 1.8 ± 0.5 nm, which could be attributed to a slight sintering of the small nanoparticles.

To evaluate the catalytic performance of Rh-C_{60} catalysts, we selected the quinoline hydrogenation, as rhodium based catalysts have shown very good performances in this reaction (Scheme 1, Table 3 and 4).[20,22,24] In addition, the fact that Rh is electron deficient, as evidenced by Raman and XPS, can be an advantage to obtain higher selectivity, as Rh-NHC carbene species[24] bearing strong donating groups on the Rh NP surface are very active for this reduction reaction working at 30°C but not very selective for the synthesis of **2.** Theoretical calculations supported our first analysis, as Rh-based catalysts intrinsically coordinate more efficiently the N-bearing ring (Table 5 $Rh_{13}H_{20}$ N *vs*. aromatic ring coordination) therefore giving preferentially the partially hydrogenated product **2**, as observed in most of the reviewed reported works. Concerning the coordination of 1,2,3,4-tetrahydroquinoline (**2**) to rhodium clusters, this difference is less pronounced (Table 6 $Rh_{13}H_{20}$ N *vs*. aromatic ring coordination), as both coordination modes are possible with similar adsorption energies (E_{ads}), and *a priori* the coordination of the aromatic group could lead to the complete hydrogenation of the molecule. As this is not so usual in the existing literature, probably steric effects should be taken into consideration, as a further coordination of another **2** molecule would give an extra stabilization, leading to a poisoning of the Rh surface by the product, an argument which is pointed out in some cases to explain the high selectivity of Rh systems.[24] We recall that full hydrogenation is possible too.[51,52] The present DFT study also endorsed our hypothesis that the use of Rh electron deficient species should be an advantage to obtain higher selectivity. Indeed, by comparing the coordination of quinoline to systems such as $Rh_{13}H_{20}$ (to mimic bare Rh NP under hydrogenation conditions), and C_{60}-$Rh_{13}H_{20}$-C_{60} (Table 5), it is observed that the hydrogenated Rh NP in interaction with fullerenes can coordinate the N-bearing aromatic ring in two distinct modes (by N, or by two carbon bonds) with similar E_{ads}. This is in contrast with the

coordination of quinoline to $Rh_{13}H_{20}$, in which the coordination of the N atom is largely favourable. This could explain the high TOF observed in the hydrogenation of quinoline using Rh-C_{60} as catalyst discussed below. The analyses of the coordination of compound **2** to the C_{60}-$Rh_{13}H_{20}$-C_{60} system (Table 6) in comparison with $Rh_{13}H_{20}$ show that in this case only the coordination by the N atom is possible, in contrast with $Rh_{13}H_{20}$ for which two coordinating modes close in adsorption energy are possible. This observation could explain the high selectivity of Rh-C_{60}, by the strong coordination of the partially hydrogenated product.

Experimentally, Rh-C_{60} catalysts were active and highly selective for the hydrogenation of the pyridine ring of the quinoline (Table 3 and 4). Using the best conditions, the selectivity towards 1,2,3,4-tetrahydroquinoline (**2**) at full conversion was in the range of 92-98% for all catalyst. Rh-C_{60} 10/1 catalyst was used to optimise the reaction conditions (Table 3). As expected, the catalytic activity increased with the temperature, the conversion of quinoline at 4 h of reaction was 44%, 65% and 100% at 60°C, 80°C and 100°C, respectively. The catalytic activity was also sensitive to the solvent, the conversion of quinoline increased following the order toluene < THF ≤ isopropanol, which is in agreement with previous works where highly polar solvents are more efficient in hydrogenation reactions with regard to low-polarity ones.[53-56] The reactions performed at 100°C reached full conversion at 3h of reaction when using isopropanol or THF as solvent and 7h in the case of toluene, with high selectivity to **2**, 97%, 97% and 95%, respectively. Reactions carried out in isopropanol and toluene were allowed to react for longer times in order to produce the fully hydrogenated product. Nevertheless, after 24 h of reaction the composition of the reaction mixture was very similar; for toluene the selectivity towards **2** at 7h (full conversion) and 24 h was the same (97%), while for isopropanol, a slight increase of the fully hydrogenated compound **4** was observed, from 1% at 3h to 5% at 24h. Time-concentration curves for the quinoline hydrogenation with Rh-C_{60} 10/1 in toluene and isopropanol are depicted in Figure S9 and S10, respectively. The high selectivity of Rh-C_{60} towards **2** is independent of the solvent used, which is in contrast with some reported systems in which the selectivity is sensible to the solvent.[26,57] Additionally, the hydrogenation of **2** and 5,6,7,8-tetrahydroquinoline (**3**) were evaluated in independent catalytic tests using Rh-C_{60} 10/1 as catalyst in isopropanol. The hydrogenation of **2** was very slow (TOF = 4.8 h^{-1}), reaching a conversion of 11% at 5 h

which remained almost unchanged at 24 h of reaction (13% conversion). On the other hand, the hydrogenation of **3** was slightly more efficient (TOF = 23.1 h^{-1}), displaying 15% at 5h and 26% at 24h of reaction.

Table 3. Selective hydrogenation of quinoline using Rh-C_{60} 10/1 nanocatalyst.[a]

Entry	T (°C)	Solvent	TOF[b] (h^{-1})	Time (h)	Conversion[c] (%)[b]	Selectivity[c] (%)		
						2	**3**	**4**
1	60	THF	19.5	1	7	100	-	-
2				4	44	98	1	1
3	80	THF	47.8	1	38	97	1	2
4				4	65	97	1	2
5	100	THF	118.6	1	75	98	1	1
6				4	100	97	1	2
7	100	toluene	99.8	1	57	97	1	2
8				4	90	98	1	1
9	100	isopropanol	123.4	1	78	98	1	1
10				4	99	97	1	2

[a] Reaction conditions: 0.02 mmol Rh, 404 mg (3.1 mmol) of quinoline, 75 mg (0.41 mmol) of dodecane (internal standard), 20 bar H_2, 25 ml of solvent. [b] TOFs calculated at 1h of reaction related to the % of Rh. [c] Conversion and selectivity determined by GC analyses using internal standard technique.

The Rh-C_{60} series was tested as catalysts in the hydrogenation of quinoline under the optimized conditions, *i.e*. using isopropanol as solvent at 100°C under 20 bar of H_2 pressure (Table 4). Time-concentration curves for the quinoline hydrogenation with the Rh-C_{60} series are given in Figure S11. In all cases, except for Rh-C_{60} 1/1, full conversion of quinoline was achieved within an hour, with high selectivity towards **2** (92-98%). The TOF were very similar among them, indicating no effect of the concentration of rhodium in both activity and selectivity. This result is in line with Raman analyses, in which similar charge transfer was evidenced for samples 5/1 to 20/1. In contrast, Rh-C_{60} 1/1 catalyst displayed the lower activity of the series, and it is probably because only a few nanoparticles are available on the surface of the nanospheres as ascertained by HRTEM analyses. The TEM analyses of the catalysts after the hydrogenation reaction showed that the nanospheres remained almost

unchanged except for Rh-C_{60} 1/1 where two populations of sizes centred at 75.0 ± 23.6 and 364.2 ± 27.8 nm (Figure S13) were observed (the mean size distribution of the as-synthesised compound was 158.2 ± 27.5 nm); indicating that these molecular species can evolve under the catalytic reaction conditions. Also, the Rh NP mean size distribution for Rh-C_{60} 5/1 and Rh-C_{60} 10/1 changed displaying a monomodal distribution but very polydisperse (Figure S13). In addition, a few isolated NP were observed in the TEM grid on the Rh-C_{60} 10/1 sample, indicating that the Rh NP are not stable on the nanosphere surface during catalysis.

Table 4. Selective hydrogenation of quinoline using Rh-C_{60} nanocatalyst.[a]

Entry	Catalyst	TOF[b] (h^{-1})	Time (h)	Conversion[c] (%)[b]	Selectivity[c] (%)		
					2	**3**	**4**
1	Rh-C_{60} 1/1	94.3	1	54	100	-	-
2			4	80	100	-	-
3	Rh-C_{60} 5/1	164.3	1	98	96	1	3
4			4	99	94	1	5
5	Rh-C_{60} 5/1 TT	157.1	1	99	97	1	3
6	Rh-C_{60} 10/1	123.4	1	78	98	1	1
7			4	99	97	1	2
8	Rh-C_{60} 20/1	157.7	1	97	92	3	5
9			4	99	90	3	7

[a] Reaction conditions: 0.02 mmol Rh, 404 mg (3.1 mmol) of quinoline, 75 mg (0.41 mmol) of dodecane (internal standard), 100 °C, 20 bar H_2, 25 ml of solvent. [b] TOFs calculated at 1h of reaction related to the % of Rh. [c] Conversion and selectivity determined by GC analyses using internal standard technique.

At first sight, no remarkable effect of the thermal treatment (TT), performed to remove adsorbed DCB, was noticed for sample Rh-C_{60} 5/1 *vs*. Rh-C_{60} 5/1 TT (Table 4 entry 3 *vs*. entry 5), although the comparison is difficult as the reaction was complete within one hour. The catalytic performances of both catalysts, Rh-C_{60} 5/1 and Rh-C_{60} 5/1 TT, were compared at lower temperature, 80°C, using smaller time intervals to analyze the reaction mixtures. Under these conditions, Rh-C_{60} 5/1 TT showed higher TOF at 15 minutes of reaction, 302.2 h^{-1}, than Rh-C_{60} 5/1, 253.8 h^{-1}. The quinoline was completely consumed within 1h and 1.5h, respectively. When the reaction was performed at 100°C using Rh-C_{60}

5/1 TT as catalyst the quinoline conversion was 94% at 15 min, reaching full conversion within 30 min (98% of selectivity towards **2**), thus a calculated TOF at 15 min of 488.0 h^{-1}, which is as high as than some other representative heterogeneous catalysts (Table S3).[17,22-24,27-29,58]

The recycling of the catalyst was investigated using Rh-C_{60} 5/1 and Rh-C_{60} 5/1 TT due to their higher activity and selectivity when compared to the rest of the series (Figure 5). Rh-C_{60} 5/1 could be reused three times without loss of catalytic activity, nevertheless, at the fourth recycling the conversion dropped to 70%. On the other hand, Rh-C_{60} 5/1 TT revealed to be more robust and was recycled five times without loss of catalytic activity. Also, TEM analyses of the Rh-C_{60} TT 5/1 catalyst after the recycling test showed no appreciable change in the nanosphere size while the Rh NP mean size increased to 2.7 ± 0.7 nm.

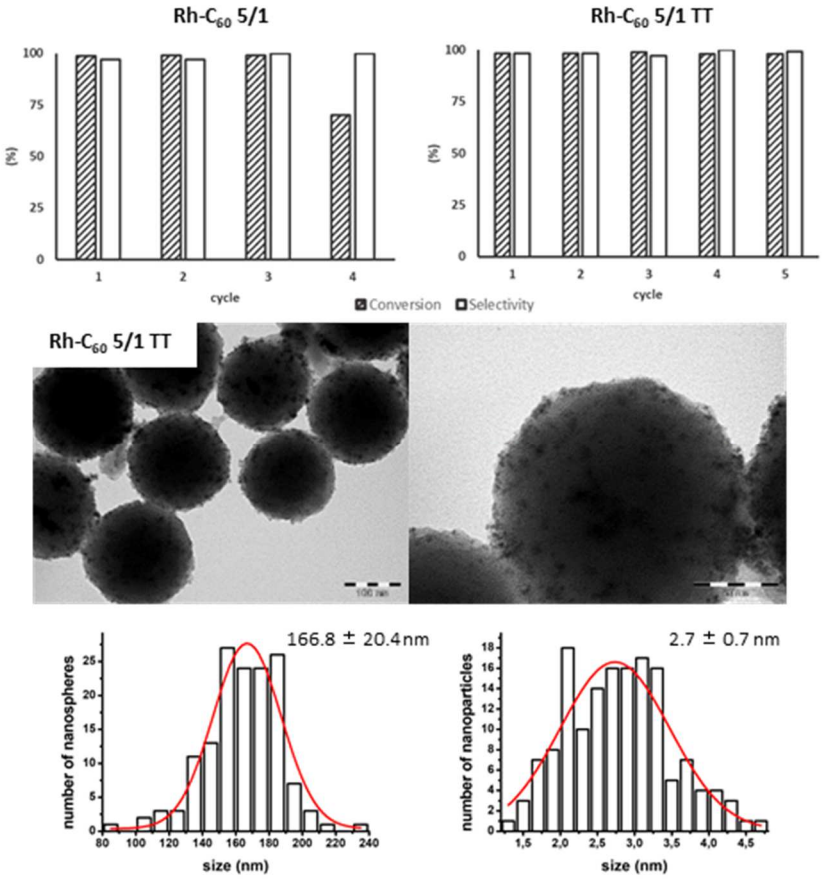

Figure 5. Conversion and selectivity for the recycling tests using Rh-C_{60} 5/1 and Rh-C_{60} 5/1 TT together with TEM images and size distribution histograms of Rh-C_{60} 5/1 TT after the recycling test (scale bar from left to right: 100 nm and 50 nm).

A DFT study has been performed in order to explore the coordination thermodynamics of quinoline (**1**) and 1,2,3,4-tetrahydroquinoline (**2**) on several Rh_{13} molecular models (Table 5 and 6). The four molecular models, denoted as supports in the tables, included bare Rh_{13} cluster, a hydride covered Rh_{13} cluster ($Rh_{13}H_{20}$), and the analogous systems with two coordinated fullerene C_{60} onto the Rh surface (C_{60}-Rh_{13}-C_{60} and C_{60}-$Rh_{13}H_{20}$-C_{60}). The coverage value of 1.7 H atom per surface Rh atom was slightly higher than the value previously used by us for Ru systems (1.5 H in $Ru_{13}H_{18}$),[31,32] since one can assume that extra hydrides with small adsorption energies are probably involved in the hydrogenation reactions. Hydrogenated Rh NP models simulate the surface of the NP under hydrogenation conditions.[59] The use of two fullerene C_{60} was chosen by analogy to our previous DFT calculations on Ru-C_{60} systems.[31,32] The adsorption energies and charge transfer of compounds **1** and **2** on those models are given after a careful check of the nature of the most stable geometries. The presence of the surface hydrides highly influences the coordination mode and the adsorption energy in both compounds. Bare Rh_{13} cluster coordinates very efficiently quinoline through π-coordination of the N-bearing aryl ring (-64 kcal/mol Rh_{13}-**1**, Table 5) while over $Rh_{13}H_{20}$ prefers to coordinate through the N atom (-25 kcal/mol $Rh_{13}H_{20}$-**1**, Table 5) and π-coordination is calculated to be very unfavourable, but possible (-9 kcal/mol $Rh_{13}H_{20}$-**1**, Table 5). Similarly, the coordination mode of **2** over Rh_{13} and $Rh_{13}H_{20}$ is largely influenced by the surface hydrides. While bare Rh_{13} cluster accommodates in a very stable way compound **2** through π-coordination of the aryl ring (-54 kcal/mol Rh_{13}-**2**, Table 6), after the addition of hydrides onto the Rh surface, this coordination is not possible leading to a coordination trough the N atom (-18 kcal/mol $Rh_{13}H_{20}$-**2**, Table 6), or through the coordination of two C atoms of the aryl ring in a η^2 position with a Rh-C distances of 2.27 and 2.42 Å, very close in adsorption energy (-17 kcal/mol $Rh_{13}H_{20}$-**2**, Table 6).

Table 5. DFT results of quinoline adsorption on several Rh_{13} clusters, comparisons between adsorption mode (N vs. aromatic ring) are highlighted and charge transfer[a] is given.

Support	Adsorption mode	E_{ads} (Kcal.mol^{-1})	Charge transfer (e$^-$)
Rh_{13}	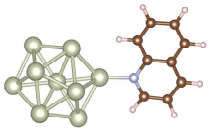	-24	+0.01
	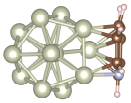	-64	+0.40
$Rh_{13}H_{20}$	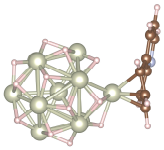	-9	-0.01
	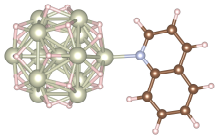	-25	-0.10
C_{60}-Rh_{13}-C_{60}	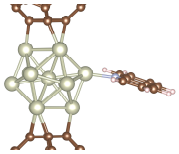	-25	-0.09
	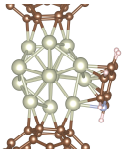	-59	+0.24
C_{60}-$Rh_{13}H_{20}$-C_{60}	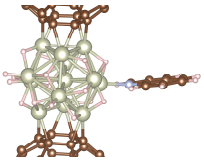	-26	-0.14
	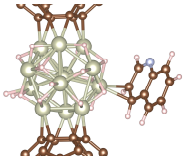	-33	+0.03

[a]Positive charge transfer means that the substrate receives electronic density from the support.

Table 6. DFT results of 1,2,3,4-tetrahydroquinoline adsorption on various supports, comparisons between adsorption mode (N vs aromatic ring) are highlighted and charge transfer[a] is given.

Support	Adsorption mode	E_{ads} (Kcal.mol^{-1})	Charge transfer (e^-)
Rh_{13}	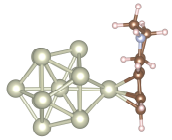	-27	-0.08
	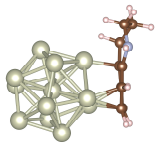	-54	+0.10
$Rh_{13}H_{20}$	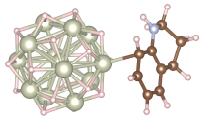	-17	-0.19
	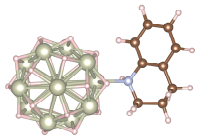	-18	-0.13
C_{60}-Rh_{13}-C_{60}	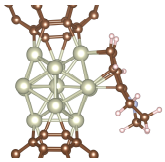	-64	-0.08
C_{60}-$Rh_{13}H_{20}$-C_{60}	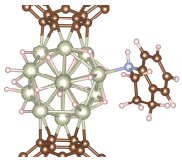	-20	-0.23

[a]Positive charge transfer means that the substrate receives electronic density from the support.

Likewise, this phenomenon is also observed in the adsorption of compound **2** on Rh_{13} clusters bearing fullerene C_{60} on their surface (π-coordination on C_{60}-Rh_{13}-C_{60} (-64 kcal/mol C_{60}-Rh_{13}-C_{60}-**2**, Table 6) vs. N-coordination on C_{60}-$Rh_{13}H_{20}$-C_{60} (-20 kcal/mol C_{60}-$Rh_{13}H_{20}$-C_{60}-**2**, Table 6)). The coordination of quinoline **1** on C_{60}-$Rh_{13}H_{20}$-C_{60} followed a slightly different trend. Even if similarly, π-coordination is not possible over the hydrogenated cluster in contrast with the highly stable π-coordination observed on

C_{60}-Rh_{13}-C_{60} (-59 kcal/mol C_{60}-Rh_{13}-C_{60}-**1**, Table 5), and N-coordination of **1** is favourable over C_{60}-$Rh_{13}H_{20}$-C_{60} (-26 kcal/mol C_{60}-$Rh_{13}H_{20}$-C_{60}-**1**, Table 5), the coordination of two carbon of the N-aryl ring to one rhodium displays a more stable adsorption energy (-33 kcal/mol C_{60}-$Rh_{13}H_{20}$-C_{60}-**1**, Table 5). As a general trend for these calculations, the hydride coverage changes the coordination mode stability. A highly stable π-coordination is observed on bare Rh_{13} clusters, whereas at high coverage ($Rh_{13}H_{20}$) N-coordination prevails. The effect of the hydride coverage could be attributed to two factors, first, they pull electronic densities from Rh atoms, and their presence on the surface impedes the π-coordination trough steric effects. This effect has been already observed by us in previous works dealing with Ru NP.[31,32]

The hydride coverage governs the coordination mode of the substrate and the partially hydrogenated product to the Rh surface, nevertheless, the presence or not of the fullerene C_{60} on the surface, also modulates the stability of the adsorbed species. In general, the addition of fullerene C_{60} decreased the charge transfer, as experimentally observed. Quinoline prefers to coordinate to the surface through a π-coordination mode of the N-bearing aryl ring in bare Rh_{13} and C_{60}-Rh_{13}-C_{60}, with a slight decrease of the adsorption energy and a change in the charge transfer (Table 5, -64 kcal/mol +0.40 e^- vs. -59 kcal/mol +0.24 e^-, respectively). Alike, the coordination of compound **2** on bare Rh_{13} and C_{60}-Rh_{13}-C_{60} displayed a similar trend, but the π-coordination on C_{60}-Rh_{13}-C_{60}, is found now more stable (Table 6, -54 kcal/mol +0.10 e^- (Rh_{13}) vs. -64 kcal/mol -0.08 e^- (C_{60}-Rh_{13}-C_{60})). The comparison of the effect of the fullerene C_{60} coordination on hydrogenated clusters allows supporting trends observed experimentally. Quinoline coordinates to the surface of $Rh_{13}H_{20}$ and C_{60}-$Rh_{13}H_{20}$-C_{60} through the N-atom displaying similar adsorption energies (-25 kcal/mol *vs*. -26 kcal/mol, Table 5), but the presence of fullerene C_{60} allowed to coordinate the quinoline trough two carbon of the N-aryl ring in a more stable way (-33 kcal/mol, Table 5), which could explain the higher activity of Rh-C_{60} compared to other reported systems (see Table S3). Also, C_{60}-$Rh_{13}H_{20}$-C_{60} accommodates compound **2** through the N-atom in a more stable manner compared to $Rh_{13}H_{20}$, which could explain that Rh-C_{60} system is highly selective. This is also supported by the fact that the coordination through the aromatic ring was found not possible in contrast with the $Rh_{13}H_{20}$. It is also noteworthy to point out that the product **2** did not poison the system for the hydrogenation of quinoline, as quinoline is coordinated more efficiently than **2** to hydrogenated

rhodium surfaces (-33 kcal/mol C_{60}-$Rh_{13}H_{20}$-C_{60}-**1**, Table 5, vs. 20 kcal/mol C_{60}-$Rh_{13}H_{20}$-C_{60}-**2**, Table 6).

CONCLUSIONS

A series of Rh-C_{60} catalysts was produced *via* a H_2 assisted solution synthesis route. Rh atomically disperse or Rh NP were prepared by tuning the molar ratio of the Rh precursor and the fullerene C_{60}. A significant interaction between Rh and C_{60} was evidenced by XPS and Raman analyses, which consisted in a charge transfer from the metal to the fullerene C_{60}. These electron-deficient Rh species are excellent catalysts for the selective reduction of quinoline to the partially hydrogenated product with selectivity up to 98%. Thermal annealing of the catalyst was highly beneficial to improve the stability of these species as seen in the recycling test, and also activity (TOF 488.0 h^{-1}), which is in between the most remarkable heterogeneous catalysts for this reaction. In addition, DFT calculations allowed pointing out the origin of the intrinsic selectivity of Rh NP-based systems when applied as catalysts in the hydrogenation of quinoline. The hydride coverage in Rh-C_{60} systems plays pivotal role and explains the origin of the high selectivity of fullerene modified Rh NP systems when applied as catalyst in the hydrogenation of quinoline.

EXPERIMENTAL SECTION

General methods. All operations were carried out under argon atmosphere using standard Schlenk techniques or in a MBraun glovebox. Solvents were purified by standard methods or by an MBraun SPS-800 solvent purification system. [Rh(η^3-C_3H_5)$_3$] was purchased from Nanomeps Toulouse, fullerene C_{60} from Bucky USA, H_2 from Air Liquide. All these reactants were used as received.

Synthesis of Rh-C_{60}. In a typical synthesis, [Rh(η^3-C_3H_5)$_3$] complex and fullerene C_{60} were placed in a Fisher-Porter bottle in a glovebox and dissolved in 1,2-dichlorobenzene (DCB). The resulting purple solution was stirred for 30 min at room temperature, pressurized with 3 bar of H_2 and then placed in a 50 ^oC oil bath. The solution turned black in few minutes and was maintained at this temperature under stirring overnight. After cooling down to room temperature, pentane was added to the reaction mixture to precipitate the Rh-C_{60} which was cleaned twice with pentane. The Rh nanoparticles were obtained as a black solid powder after drying under vacuum overnight. For each ratio studied, the

quantities of reactants are detailed hereafter:

Rh-C_{60} 1/1: 50 mg (0.22 mmol) of [Rh(η^3-C_3H_5)$_3$]; 160 mg (0.22 mmol) of fullerene C_{60} and 100 mL of DCB. Yield: 160 mg. Rh content: 9.2 %

Rh-C_{60} 5/1: 25 mg (0.11 mmol) of [Rh(η^3-C_3H_5)$_3$]; 16 mg (0.02 mmol) of fullerene C_{60} and 10 mL of DCB. Yield: 20 mg. Rh content: 23.3 %

Rh-C_{60} 10/1: 100 mg (0.44 mmol) of [Rh(η^3-C_3H_5)$_3$]; 32 mg (0.04 mmol) of fullerene C_{60} and 20 mL of DCB. Yield: 100 mg. Rh content: 35.9 %

Rh-C_{60} 20/1: 200 mg (0.86 mmol) of [Rh(η^3-C_3H_5)$_3$]; 32 mg (0.04 mmol) of fullerene C_{60} and 20 mL of DCB. Yield: 75 mg. Rh content: 46.2 %

Growth mechanism. The reaction was performed at -20 °C following the standard procedure: 50 mg (0.22 mmol) of [Rh(η^3-C_3H_5)$_3$]] 16 mg (0.02 mmol) of fullerene C_{60} and 10 mL of DCB. The reaction was followed by sampling the mixture over the time.

General procedure for the hydrogenation of quinoline. The hydrogenation of quinoline was performed in a 40 ml stainless steel high-pressure batch BR-25 Berghof reactor. Typically, a mixture of Rh-C_{60} catalysts (0.02 mmol Rh), dodecane (75 mg; 0.44 mmol) and quinoline (404 mg, 3.12 mmol) in 25 ml of the desired solvent were loaded into the autoclave in the glovebox. The autoclave was purged three times with H_2 to remove the inert atmosphere; heated to 100 ^oC and charged with 20 bar of H_2. The stirring rate was fixed at 1500 rpm. Samples of the reaction mixture were taken at different time intervals and analysed by gas chromatography. Quantitative analyses of reaction mixtures were performed via GC using calibration solutions of commercially available products.

Catalytic recycling tests. A mixture of quinoline (404 mg, 3.10 mmol), dodecane (75mg, 0.41 mmol), Rh-C_{60} 5/1 catalysts (0.02 mmol Rh) and 25 ml of isopropanol was prepared in the glovebox and introduced into the autoclave. The autoclave was purged three times with H_2; heated to 100 ^oC and pressurized with 20 bar of H_2 during 1 h keeping the stirring rate at 1500 rpm. After the reaction, the catalyst was recovered into a Schlenck tube by filtrating with a cannula and washing several times with

EtOH under argon, and then dried under vacuum. The catalyst was reused in another five cycles of the hydrogenation reaction following the procedure described above.

TEM analyses. TEM and HRTEM analyses were performed at the "Centre de microcaracterisation Raimond Castaing, UMS 3623, Toulouse" by using a JEOL JEM 1011 CXT electron microscope operating at 100 kV with a point resolution of 4.5 Å. The high resolution analyses were conducted using a JEOL JEM 2100F equipped with a Field Emission Gun (FEG) operating at 200 kV with a point resolution of 2.3 Å and a JEOL JEM-ARM200F Cold FEG operating at 200 kV with a point resolution of >1.9 Å. The approximation of the particles mean size was stablished through a manual analysis of enlarged micrographs by measuring at least 200 particles on a given grid. Other TEM micrographs were acquired with a JEOL 2100F S/TEM microscope equipped with a FEG operating at 200 kV, a spherical aberration probe corrector and a GATAN Tridiem energy filter. The resolutions attained are 2 Å and 1.1 Å under parallel TEM mode and scanning STEM modes, respectively. For STEM-HAADF analyses the spot size was of 0.13 nm, a current density of 140 pA, the camera focal length was 10 cm, corresponding to inner and outer detection angle of the annular detector of about 60 mrad and 160 mrad.

WAXS analyses. Wide Angle X-ray Scattering measurements were performed at CEMES on a diffractometer dedicated to Pair Distribution Function (PDF) analysis: graphite-monochromatized Molybdenum radiation (0.07169nm), solid-state detection and low background setup. Samples were sealed in Lindemann glass capillaries (diameter 1 mm) to avoid any oxidation after filling in a glove box. For all samples data were collected on an extended angular range (129 degrees in 2theta) with counting times of typically 150s for each of the 457 data points, thus allowing for PDF analysis. Classic corrections (polarization and absorption in cylindrical geometry) were applied before reduction and Fourier transform.

ICP analyses. The rhodium content was established by inductively coupled plasma optical emission spectroscopy (ICP-OES) performed at the LCC in a Thermo Scientific ICAP 6300 instrument after acid mineralization of the samples.

Raman analyses. Raman measurements were carried out with a Horiba XPLORA-MV2000 spectrometer. For the measurements, an excitation wavelength of 532 nm and laser power of 0.084 mW was used. The samples were kept under vacuum and exposed to atmospheric air shortly before measurements.

XPS analyses. XPS measurements were performed on a Thermo Kα spectrometer working at a base pressure of $5x10^{-9}$ mbars and equipped with a monochromatic Al Kα X-ray source (1486.7 eV). The spectra presented here were recorded with a Pass Energy of 20 eV. The data were processed with CasaXPS using Gaussian-lorentzian combinations and a Shirley background. Scofield photoionization cross-sections[60] corrected for the transmission function of the analyzer and the analysis depth were used for quantifications.

ATR-IR. ATR-IR spectra were recorded on a Perkin-Elmer GX2000 spectrometer available in a glovebox, in the range 4000-400 cm^{-1}.

SSNMR. Solid state NMR (MAS-NMR) with and without ^{1}H-^{13}C cross polarization (CP) were performed at the LCC on a Bruker Avance 400WB instrument equipped with a 4 mm probe with the sample rotation frequency being set at 12 kHz unless otherwise indicated. Measurements were carried out in a 4 mm ZrO_2 rotor.

TGA. Thermal analysis under air were performed in a Thermobalance Perkin Elmer Diamond TG.

GC analyses. GC analyses were performed in a PerkinElmer Autosystem GC equipped with an Elite-5MS Capillary Column (30 m × 0.25 mm × 0.25 μm). Split (20:1); carrier gas flow: He, 20 ml/min; injector temperature: 250 °C; detector (FID) temperature: 250 °C; oven program: 110 °C (hold 12 min) to 230 °C at 20 °C/min (hold 3 min) for a total run time of 21 min; retention time: dodecane, 5.3 min; **1**, 7.0 min; **2**, 11.3 min; **3**, 6.5 min; and **4**, 4.4 min.

Computational details. DFT calculations were performed using the Vienna *ab initio* simulation package VASP,[61-64] based on the full-potential projector augmented wave framework.[65,66] Exchange-correlation effects have been approximated using the spin-polarized version of PBE functional.[67] A kinetic-energy

cutoff of 400 eV was found to be sufficient to achieve a total-energy convergence within several meV, considering the k-point sampling in Gamma-point only calculations for isolated molecules and complexes, in conjunction with a Gaussian smearing with a width of 0.05 eV. During geometry optimization runs, all the atoms were fully relaxed until forces on individual atoms were smaller than 0.01 eV/Å. Calculation cells for isolated molecules and complexes were (25x26x27) $Å^3$, to avoid spurious interactions between periodic images. Figures of the different geometries were produced thanks to the 3D visualization program VESTA.[68] Bader charge analyses were performed using Henkelmann's group code.[69] The optimal geometries upon H_2 adsorption were constructed following the results of Ref.,[70] *i. e.* all available μ_3 sites were occupied and then the top sites and, if needed, some bridge sites were used to build the starting geometries.

ACKNOWLEDGMENTS

This work was supported by the Centre National de la Recherche Scientifique (CNRS), which we gratefully acknowledge. I.C.G. acknowledges the Calcul en Midi-Pyrénées initiative CALMIP (Project p0812) for allocations of computer time.

REFERENCES

(1) Johnstone, R. A.; Wilby, A. H.; Entwistle, I. D.: Heterogeneous catalytic transfer hydrogenation and its relation to other methods for reduction of organic compounds. *Chem. Rev.* **1985**, *85*, 129-170.

(2) Blaser, H. U.; Malan, C.; Pugin, B.; Spindler, F.; Steiner, H.; Studer, M.: Selective hydrogenation for fine chemicals: recent trends and new developments. *Adv. Synth. Catal.* **2003**, *345*, 103-151.

(3) Gilkey, M. J.; Xu, B.: Heterogeneous catalytic transfer hydrogenation as an effective pathway in biomass upgrading. *ACS Catal.* **2016**, *6*, 1420-1436.

(4) Meemken, F.; Baiker, A.: Recent progress in heterogeneous asymmetric hydrogenation of C=O and C=C bonds on supported noble metal catalysts. *Chem. Rev.* **2017**, *117*, 11522-11569.

(5) Jia, J.; Qian, C.; Dong, Y.; Li, Y. F.; Wang, H.; Ghoussoub, M.; Butler, K. T.; Walsh, A.; Ozin, G. A.: Heterogeneous catalytic hydrogenation of CO_2 by metal oxides: defect engineering–perfecting imperfection. *Chem. Soc. Rev.* **2017**, *46*, 4631-4644.

(6) Wildgoose, G. G.; Banks, C. E.; Compton, R. G.: Metal nanoparticles and related materials supported on carbon nanotubes: methods and applications. *Small* **2006**, *2*, 182-193.

(7) Li, X.-H.; Antonietti, M.: Metal nanoparticles at mesoporous N-doped carbons and carbon nitrides: functional Mott–Schottky heterojunctions for catalysis. *Chem. Soc. Rev.* **2013**, *42*, 6593-6604.

(8) Zhai, Y.; Zhu, Z.; Dong, S.: Carbon-based nanostructures for advanced catalysis. *ChemCatChem* **2015**, *7*, 2806-2815.

(9) Cui, X.; Surkus, A.-E.; Junge, K.; Topf, C.; Radnik, J.; Kreyenschulte, C.; Beller, M.: Highly selective hydrogenation of arenes using nanostructured ruthenium catalysts modified with a carbon–nitrogen matrix. *Nat.*

Commun. **2016**, *7*, 11326pp.

(10) Navalon, S.; Dhakshinamoorthy, A.; Alvaro, M.; Garcia, H.: Metal nanoparticles supported on two-dimensional graphenes as heterogeneous catalysts. *Coord. Chem. Rev.* **2016**, *312*, 99-148.

(11) Perez-Mayoral, E.; Calvino-Casilda, V.; Soriano, E.: Metal-supported carbon-based materials: opportunities and challenges in the synthesis of valuable products. *Catal. Sci. Technol.* **2016**, *6*, 1265-1291.

(12) Zhang, H.; Yan, X.; Huang, Y.; Zhang, M.; Tang, Y.; Sun, D.; Xu, L.; Wei, S.: Cyanogel-derived N-doped C nanosheets immobilizing Pd-P nanoparticles: One-pot synthesis and enhanced hydrogenation catalytic performance. *Appl. Surf. Sci.* **2017**, *396*, 812-820.

(13) Shuman, R. T.; Ornstein, P. L.; Paschal, J. W.; Gesellchen, P. D.: An improved synthesis of homoproline and derivatives. *J. Org. Chem.* **1990**, *55*, 738-741.

(14) Katritzky, A. R.; Rachwal, S.; Rachwal, B.: Recent progress in the synthesis of 1,2,3,4,-tetrahydroquinolines. *Tetrahedron* **1996**, *52*, 15031-15070.

(15) Sridharan, V.; Suryavanshi, P. A.; Menéndez, J. C.: Advances in the chemistry of tetrahydroquinolines. *Chem. Rev.* **2011**, *111*, 7157-7259.

(16) Keay, J. D.: In *Comprehensive Organic Synthesis, Vol. 8*; Trost, B. M., Fleming, I., Eds.; Pergamon, Oxford, 1991; pp 579- 601.

(17) Ren, D.; He, L.; Yu, L.; Ding, R.-S.; Liu, Y.-M.; Cao, Y.; He, H.-Y.; Fan, K.-N.: An unusual chemoselective hydrogenation of quinoline compounds using supported gold catalysts. *J. Am. Chem. Soc.* **2012**, *134*, 17592-17598.

(18) Park, I. S.; Kwon, M. S.; Kang, K. Y.; Lee, J. S.; Park, J.: Rhodium and iridium nanoparticles entrapped in aluminum oxyhydroxide nanofibers: catalysts for hydrogenations of arenes and ketones at room temperature with hydrogen balloon. *Adv. Synth. Catal.* **2007**, *349*, 2039-2047.

(19) Mao, H.; Liao, X.; Shi, B.: Amphiphilic tannin-stabilized Rh nanoparticles: A highly active and reusable catalyst in biphasic aqueous-organic system. *Catal. Commun.* **2011**, *16*, 210-214.

(20) Fan, G.-Y.; Wu, J.: Mild hydrogenation of quinoline to decahydroquinoline over rhodium nanoparticles entrapped in aluminum oxy-hydroxide. *Catal. Comm.* **2013**, *31*, 81-85.

(21) Jiang, H.-Y.; Zheng, X.-X.: Phosphine-functionalized ionic liquid-stabilized rhodium nanoparticles for selective hydrogenation of aromatic compounds. *Appl. Catal., A* **2015**, *499*, 118-123.

(22) Niu, M.; Wang, Y.; Chen, P.; Du, D.; Jiang, J.; Jin, Z.: Highly efficient and recyclable rhodium nanoparticle catalysts for hydrogenation of quinoline and its derivatives. *Catal. Sci. Technol.* **2015**, *5*, 4746-4749.

(23) Karakulina, A.; Gopakumar, A.; Akçok, İ.; Roulier, B. L.; LaGrange, T.; Katsyuba, S. A.; Das, S.; Dyson, P. J.: A rhodium nanoparticle–lewis acidic ionic liquid catalyst for the chemoselective reduction of heteroarenes. *Angew. Chem., Int. Ed.* **2016**, *128*, 300-304.

(24) Martinez-Espinar, F.; Blondeau, P.; Nolis, P.; Chaudret, B.; Claver, C.; Castillón, S.; Godard, C.: NHC-stabilised Rh nanoparticles: Surface study and application in the catalytic hydrogenation of aromatic substrates. *J. Catal.* **2017**, *354*, 113-127.

(25) Karakulina, A.; Gopakumar, A.; Fei, Z.; Dyson, P. J.: Chemoselective reduction of heteroarenes with a reduced graphene oxide supported rhodium nanoparticle catalyst. *Catal. Sci. Technol.* **2018**, *8*, 5091-5097.

(26) Zhang, L.; Wang, X.; Xue, Y.; Zeng, X.; Chen, H.; Li, R.; Wang, S.: Cooperation between the surface hydroxyl groups of Ru–SiO_2@ mSiO_2 and water for good catalytic performance for hydrogenation of quinoline. *Catal. Sci. Technol.* **2014**, *4*, 1939-1948.

(27) Konnerth, H.; Prechtl, M. H. G.: Selective hydrogenation of N-heterocyclic compounds using Ru nanocatalysts in ionic liquids. *Green Chem.* **2017**, *19*, 2762-2767.

(28) Dell'Anna, M. M.; Capodiferro, V. F.; Mali, M.; Manno, D.; Cotugno, P.; Monopoli, A.; Mastrorilli, P.: Highly selective hydrogenation of quinolines promoted by recyclable polymer supported palladium nanoparticles

under mild conditions in aqueous medium. *Appl. Catal., A.* **2014**, *481*, 89-95.

(29) Bai, L.; Wang, X.; Chen, Q.; Ye, Y.; Zheng, H.; Guo, J.; Yin, Y.; Gao, C.: Explaining the size dependence in platinum-nanoparticle-catalyzed hydrogenation reactions. *Angew. Chem., Int. Ed.* **2016**, *55*, 15656-15661.

(30) Leng, F.; Gerber, I. C.; Lecante, P.; Bacsa, W.; Miller, J.; Gallagher, J. R.; Moldovan, S.; Girleanu, M.; Axet, M. R.; Serp, P.: Synthesis and structure of ruthenium-fullerides. *RSC Advances* **2016**, *6*, 69135-69148.

(31) Leng, F.; Gerber, I. C.; Lecante, P.; Moldovan, S.; Girleanu, M.; Axet, M. R.; Serp, P.: Controlled and chemoselective hydrogenation of nitrobenzene over Ru@C_{60} catalysts. *ACS Catal.* **2016**, *6*, 6018-6024.

(32) Axet, M. R.; Conejero, S.; Gerber, I. C.: Ligand effects on the selective hydrogenation of nitrobenzene to cyclohexylamine using ruthenium nanoparticles as catalyst. *ACS Appl. Nano Mater.* **2018**, *1*, 5885-5894.

(33) Amiens, C.; Ciuculescu-Pradines, D.; Philippot, K.: Controlled metal nanostructures: Fertile ground for coordination chemists. *Coord. Chem. Rev.* **2016**, *308*, 409-432.

(34) Coq, B.; Planeix, J. M.; Brotons, V.: Fullerene-based materials as new support media in heterogeneous catalysis by metals. *Appl. Catal., A.* **1998**, *173*, 175-183.

(35) Veisi, H.; Masti, R.; Kordestani, D.; Safaei, M.; Sahin, O.: Functionalization of fullerene (C_{60}) with metformine to immobilized palladium as a novel heterogeneous and reusable nanocatalyst in the Suzuki–Miyaura coupling reaction at room temperature. *J. Mol. Catal. A: Chem* **2014**, *385*, 61-67.

(36) Keypour, H.; Noroozi, M.; Rashidi, A.: Schiff base complex method for the preparation of gullerene-based Ni nanocatalyst used in the hydrogenation of benzene in gasoline. *Synth. React. Inorg. Met. Org. Chem.* **2015**, *45*, 1701-1709.

(37) Braun, T.; Wohlers, M.; Belz, T.; Schlögl, R.: Fullerene-based ruthenium catalysts: a novel approach for anchoring metal to carbonaceous supports. II. Hydrogenation activity. *Catal. Lett.* **1997**, *43*, 175-180.

(38) Lashdaf, M.; Hase, A.; Kauppinen, E.; Krause, A. O. I.: Fullerene-based ruthenium catalysts in cinnamaldehyde hydrogenation. *Catal. Lett.* **1998**, *52*, 199-204.

(39) Axet, M. R.; Dechy-Cabaret, O.; Durand, J.; Gouygou, M.; Serp, P.: Coordination chemistry on carbon surfaces. *Coord. Chem. Rev.* **2016**, *308*, 236-345.

(40) Mabille, C.; Leal-Calderon, F.; Bibette, J.; Schmitt, V.: Monodisperse fragmentation in emulsions: mechanisms and kinetics. *Europhys. Lett.* **2003**, *61*, 708-714.

(41) Osborn, J. A.; Schrock, R. R.: Coordinatively unsaturated cationic complexes of rhodium(I), iridium(I), palladium(II), and platinum(II). Generation, synthetic utility, and some catalytic studies. *J. Amer. Chem. Soc.* **1971**, *93*, 3089-91.

(42) Green, M.; Kuc, T. A.: Cationic transition-metal complexes. II. Reaction of arenes and olefins with bis(1,5-cyclooctadiene or norbornadiene)rhodium tetrafluoroborate. *J. Chem. Soc., Dalton Trans.* **1972**, 832-9.

(43) Uson, R.; Oro, L. A.; Foces-Foces, C.; Cano, F. H.; Garcia-Blanco, S.; Valderrama, M.: Arene-rhodium(I) complexes with trimethyltetrafluorobenzobarrelene. Crystal structure of [(Me_3TFB)Rh(p-$Me_2C_6H_4$)]ClO_4. *J. Organomet. Chem.* **1982**, *229*, 293-304.

(44) Abe, Y.; Kato, K.; Kawamura, M.; Sasaki, K.: Rhodium and rhodium oxide thin films characterized by XPS. *Surf. Sci. Spectra* **2001**, *8*, 117-125.

(45) Tsuei, K.-D.; Yuh, J.-Y.; Tzeng, C.-T.; Chu, R.-Y.; Chung, S.-C.; Tsang, K.-L.: Photoemission and photoabsorption study of C_{60} adsorption on Cu(111) surfaces. *Phys. Rev. B: Condens. Matter* **1997**, *56*, 15412-15420.

(46) Dresselhaus, M. S.; Dresselhaus, G.; Eklund, P. C.: Raman scattering in fullerenes. *J. Raman Spectrosc.* **1996**, *27*, 351-371.

(47) Chen, X. H.; Zhou, X. J.; Roth, S.: Raman scattering in calcium-doped C_{60}. *Phys. Rev. B: Condens. Matter* **1996**, *54*, 3971-3975.

(48) Jishi, R. A.; Dresselhaus, M. S.: Mode softening and mode stiffening in C_{60} doped with alkali metals. *Phys. Rev. B Condens. Matter.* **1992**, *45*, 6914-6918.

(49) Sakai, S.; Naramoto, H.; Avramov, P. V.; Yaita, T.; Lavrentiev, V.; Narumi, K.; Baba, Y.; Maeda, Y.: Comparative study of structures and electrical properties in cobalt-fullerene mixtures by systematic change of cobalt content. *Thin Solid Films* **2007**, *515*, 7758-7764.

(50) Becker, L.; Evans, T. P.; Bada, J. L.: Synthesis of [hydrogenated fullerene] $C_{60}H_2$ by rhodium-catalyzed hydrogenation of C_{60}. *J. Org. Chem.* **1993**, *58*, 7630-1.

(51) Chaudhari, C.; Imatome, H.; Nishida, Y.; Sato, K.; Nagaoka, K.: Recyclable Rh-PVP nanoparticles catalyzed hydrogenation of benzoic acid derivatives and quinolines under solvent-free conditions. *Catal. Commun.* **2019**, *126*, 55-60.

(52) Mateen, M.; Shah, K.; Chen, Z.; Chen, C.; Li, Y.: Selective hydrogenation of N-heterocyclic compounds over rhodium-copper bimetallic nanocrystals under ambient conditions. *Nano Res.* **2019**, *12*, 1631-1634.

(53) Wei, Z.; Chen, Y.; Wang, J.; Su, D.; Tang, M.; Mao, S.; Wang, Y.: Cobalt encapsulated in N-doped graphene layers: an efficient and stable catalyst for hydrogenation of quinoline compounds. *ACS Catal.* **2016**, *6*, 5816-5822.

(54) Sun, Y.-P.; Fu, H.-Y.; Zhang, D.-l.; Li, R.-X.; Chen, H.; Li, X.-J.: Complete hydrogenation of quinoline over hydroxyapatite supported ruthenium catalyst. *Catal. Comm.* **2010**, *12*, 188-192.

(55) Gong, Y.; Zhang, P.; Xu, X.; Li, Y.; Li, H.; Wang, Y.: A novel catalyst Pd@ ompg-C_3N_4 for highly chemoselective hydrogenation of quinoline under mild conditions. *J. Catal.* **2013**, *297*, 272-280.

(56) Sánchez-Delgado, R. A.; Machalaba, N.: Hydrogenation of quinoline by ruthenium nanoparticles immobilized on poly (4-vinylpyridine). *Catal. Comm.* **2007**, *8*, 2115-2118.

(57) Sun, B.; Khan, F.-A.; Vallat, A.; Süss-Fink, G.: NanoRu@ hectorite: a heterogeneous catalyst with switchable selectivity for the hydrogenation of quinoline. *Appl. Catal., A.* **2013**, *467*, 310-314.

(58) Mao, H.; Ma, J.; Liao, Y.; Zhao, S.; Liao, X.: Using plant tannin as natural amphiphilic stabilizer to construct an aqueous-organic biphasic system for highly active and selective hydrogenation of quinoline. *Catal. Sci. Technol.* **2013**, *3*, 1612-1617.

(59) Martinez-Prieto, L. M.; Chaudret, B.: Organometallic ruthenium nanoparticles: synthesis, surface chemistry, and insights into ligand coordination. *Acc. Chem. Res.* **2018**, *51*, 376-384.

(60) Scofield, J. H.: Hartree-Slater subshell photoionization cross-sections at 1254 and 1487 eV. *J. Electron Spectrosc. Relat. Phenom.* **1976**, *8*, 129-37.

(61) Kresse, G.; Furthmüller, J.: Efficiency of ab-initio total energy calculations for metals and semiconductors using a plane-wave basis set. *Comput. Mater. Sci.* **1996**, *6*, 15-50.

(62) Kresse, G.; Hafner, J.: Ab initio molecular dynamics for liquid metals. *Phys. Rev. B* **1993**, *47*, 558-561.

(63) Kresse, G.; Furthmüller, J.: Efficient iterative schemes for *ab initio* total-energy calculations using a plane-wave basis set. *Phys. Rev. B* **1996**, *54*, 11169-11186.

(64) Kresse, G.; Hafner, J.: Ab initio molecular-dynamics simulation of the liquid-metal–amorphous-semiconductor transition in germanium. *Phys. Rev. B* **1994**, *49*, 14251-14269.

(65) Blöchl, P. E.: Projector augmented-wave method. *Phys. Rev. B* **1994**, *50*, 17953-17979.

(66) Kresse, G.; Joubert, D.: From ultrasoft pseudopotentials to the projector augmented-wave method. *Phys. Rev. B* **1999**, *59*, 1758-1775.

(67) Perdew, J. P.; Burke, K.; Ernzerhof, M.: Generalized gradient approximation made simple. *Phys. Rev. Lett.* **1996**, *77*, 3865-3868.

(68) Momma, K.; Izumi, F.: VESTA 3 for three-dimensional visualization of crystal, volumetric and morphology data. *J. Appl. Crystallogr.* **2011**, *44*, 1272-1276.

(69) Tang, W.; Sanville, E.; Henkelman, G.: A grid-based Bader analysis algorithm without lattice bias. *J. Phys.:*

Condens. Matter **2009**, *21*, 084204/1-084204/7.

(70) del Rosal, I.; Truflandier, L.; Poteau, R.; Gerber, I. C.: A density functional theory study of spectroscopic and thermodynamic properties of surfacic hydrides on Ru (0001) model surface: the influence of the coordination modes and the coverage. *J. Phys. Chem. C* **2011**, *115*, 2169-2178.